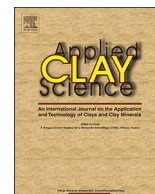




Contents lists available at ScienceDirect

Applied Clay Science

journal homepage: www.elsevier.com/locate/clay

Research paper

Microbially induced palygorskite-sepiolite authigenesis in modern hypersaline lakes (Central Spain)

Pablo del Buey^{a,*}, Óscar Cabestrero^a, Xabier Arroyo^b, M. Esther Sanz-Montero^a^a Department of Petrology and Geochemistry, Faculty of Geological Sciences, Complutense University of Madrid, Calle José Antonio Novais 12, 28040 Madrid, Spain^b CAI de Técnicas Geológicas, Facultad de Ciencias Geológicas, Universidad Complutense de Madrid, C/José Antonio Novais, 12, 28040 Madrid, Spain

ARTICLE INFO

Keywords:

Palygorskite
 Sepiolite
 Microbial mats
 Authigenesis
 EPS dehydration

ABSTRACT

This study gives insight into the mechanisms of formation of palygorskite-sepiolite minerals that have remained elusive for many years. The occurrence of palygorskite-sepiolite and minor smectite in association with a variety of authigenic sulphates and Ca-Mg carbonate mineral deposits was identified in silicon-poor, saline to hypersaline ephemeral lakes in Central Spain. By a combination of sedimentological, mineralogical and petrological techniques (XRD, SEM, FEGSEM and TEM) it is shown that very small, poorly ordered palygorskite-sepiolite crystals resulted from the aggregation of nanocrystals within the matrix of the microbial mats (EPS) as it dehydrates. The Mg-rich clays nucleated on Mg-enriched EPS that also contain variable amounts of Si, Mg, Al and Fe, mostly derived from the degradation of siliciclastic minerals. The crystals have a broad compositional and textural range, from poorly ordered palygorskite laths to pure sepiolite bundles, suggesting that they grow through successive stages. Changes in the chemical composition of the fibers occur even at microscale, which is explained by the variability of the biogeochemical conditions prevailing in the microenvironments where the crystals grow. The overall results provide evidence for a biomediated-crystallization of palygorskite-sepiolite in microbial sediments.

1. Introduction

The occurrence and authigenic formation of Mg-rich clay minerals is widely reported in literature of ancient lacustrine rocks (Calvo et al., 1999; Galán and Pozo, 2011; Calvo and Pozo, 2013). However, detailed descriptions of Mg-rich authigenic clays and more specifically sepiolite and palygorskite in modern lacustrine environments are uncommon, thus the interpretation of their environmental formative controls has relied on laboratory experiments (Birsoy, 2002; Tosca and Masterson, 2014) or the analyses of sedimentary sequences (Bustillo Revuelta and García-Romero, 2003). The mechanisms commonly invoked for the formation of the authigenic clays in these environments are the transformation of a mineral precursor through dissolution-precipitation (Suárez et al., 1994) and the neoformation by direct precipitation from brines or pore fluids (Khademi and Mermut, 1998; Pozo and Casas, 1999; Galán and Pozo, 2011).

Alternatively, several lines of evidence suggest a biological-assisted nucleation of palygorskite and/or sepiolite minerals in ancient microbialites (Sanz-Montero et al., 2008; Leguey et al., 2010; Cuevas et al., 2011), which agrees with the increasing observations of authigenic magnesium silicates in modern lacustrine microbialites (Ferris et al.,

1987; Cabestrero et al., 2014a; Zeyen et al., 2015). Along this line, Cabestrero et al. (2014a) reported palygorskite and sepiolite authigenesis in microbial mats hosted in playa lakes from Central Spain. In these shallow lakes, water availability and composition (salinity, pH, Eh, etc.) as well as the microbial composition and mineralogy change drastically through the year (Sanz-Montero et al., 2013b; Cabestrero et al., 2013; Sanz-Montero et al., 2015a; Cabestrero and Sanz-Montero, 2018; Cabestrero et al., 2018). Likely due to this variability, few studies have addressed the authigenesis of palygorskite and sepiolite in modern playa lakes, despite they are the most favorable sedimentary environments (Jones, 1983; Singer, 1989; Sánchez and Galán, 1995; Galán and Pozo, 2011) and are conspicuous worldwide (Navarro et al., 2008).

The deposition of Mg-rich clays in playa lake deposits from Central Spain provide a good opportunity for characterizing sepiolite and palygorskite minerals, by a combination of sedimentary, mineralogical, geochemical and microscopic techniques. In addition, this study aimed to investigate vertical and lateral variability of the clays in relation with microbial mats, hydrochemistry and detrital mineral paragenesis to constrain the mechanisms involved in the authigenesis of sepiolite and palygorskite minerals.

* Corresponding author.

E-mail address: pabodelbuey@ucm.es (P. del Buey).<https://doi.org/10.1016/j.clay.2018.02.020>Received 26 September 2017; Received in revised form 9 February 2018; Accepted 14 February 2018
 0169-1317/ © 2018 Elsevier B.V. All rights reserved.

2. Environmental setting

2.1. Geomorphology and geology

The studied lakes are permanent (Longar, LG) and temporal lakes (Alttillo Chica, AC and Alttillo Grande, AG) that are located in a hydrologically closed wetland in La Mancha region (Central Spain) (Fig. 1). These three mesosaline to hypersaline lakes have no inflow from major rivers and insignificant groundwater contribution, so surface water runoff comes mainly from rainwater. The region has a continental semi-arid climate and is characterized by a high evaporation ($1300\text{--}1660\text{ mm}\cdot\text{yr}^{-1}$) and low precipitation ($360\text{--}500\text{ mm}\cdot\text{yr}^{-1}$). The annual mean temperature is 14°C , and extreme values of -7°C and 40°C are registered in January and July, respectively (Cabestrero and Sanz-Montero, 2018).

AG and AC are 0.20 and 0.17 km^2 playas at an elevation of 678 and 682 m , respectively (Fig. 1). Over the winter, the nearly-flat surfaces in the center of the playa lakes are unevenly covered by a thin sheet of water. The water column reached up to 0.25 m , but used to be $< 0.05\text{ m}$ deep on average (Sanz-Montero et al., 2015b; Cabestrero and Sanz-Montero, 2018). They are considered seasonal lakes, drying out completely from May to September. In contrast, Longar Lake is a permanent lake with a large surface of 0.91 km^2 , lying at 683 m , and filled with an averaged water column between 0.35 m (winter-spring) and 0.10 m (late summer). The lakes lie on horizontally-bedded Neogene sedimentary rocks that consist of gypsum, chert, carbonates and quartzitic sandstone and conglomerates (Sanz-Montero et al., 2015a).

2.2. Hydrochemistry

The brines are usually of $\text{Mg}^{2+}\text{--}(\text{Na}^+)\text{--}(\text{Ca}^{2+})\text{--}\text{SO}_4^{2-}\text{--}(\text{Cl}^-)$ type (Cabestrero and Sanz-Montero, 2018). AG has the highest $\text{SO}_4^{2-}/\text{Cl}^-$ ratio resulting in a $\text{Mg}^{2+}\text{--}\text{SO}_4^{2-}$ composition. In contrast, AC has $\text{Mg}^{2+}\text{--}\text{Cl}^-$ brines, and Longar is in between with a $\text{Mg}^{2+}\text{--}\text{SO}_4^{2-}\text{--}\text{Cl}^-$ composition. They have high to very high molar $\text{Mg}^{2+}/\text{Ca}^{2+}$ averaged ratios such as 5 in AG, 33 in AC and 58 in Longar. Na^+/Cl^- ratios range from 1.82 to 0.67 in AG, 0.86 to 0.62 in AC and 0.97 to 0.34 in LG.

2.3. Sedimentary features

The bed material has an average composition of gypsum precipitates

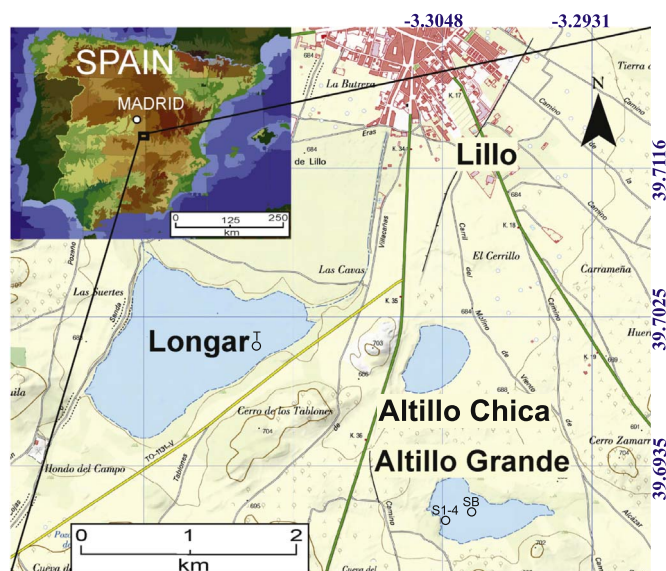


Fig. 1. Location map of the studied playa lakes (Longar, Alttillo Chica and Alttillo Grande) at the south of Lillo village in La Mancha region, Spain. Situation of the trench and cores are represented by circles (T, S1–4, SB).

(up to 75%), clastic material and clays and up to 4% of organic constituents. Gypsum crystallizes as lenticular crystals that can be replaced by minor celestite microcrystals (Sanz-Montero et al., 2009a, 2013a). Clastic sediments consist mainly of silt-sized quartz, feldspars, carbonates and up to 30% of clay minerals (Cabestrero et al., 2014a).

In the spring, the sediment gets covered by cohesive microbial mats. In the most surficial layer of the mats, the exopolymeric substances (EPS) excreted by the microorganisms (cyanobacteria and diatoms) form a tight framework in which the detrital and authigenic minerals are firmly held (Sanz-Montero and Rodríguez-Aranda, 2013). Extensive growth of microbial mats on the bed enhances the formation of microbial mat-related structures, including different construction, deformation and destruction forms (Sanz-Montero et al., 2013b, 2015a). In addition, microbial mats modify the chemical behavior of the brine and promote the precipitation of carbonates and sulphates, despite unfavorable saturation conditions for most of them (Cabestrero and Sanz-Montero, 2018; Cabestrero et al., 2018). Authigenic carbonates as calcite, aragonite, and minor dolomite, hydromagnesite, monohydrocalcite, magnesite and nesquehonite can also be found precipitating within the microbial mats (Cabestrero and Sanz-Montero, 2018).

In the late spring, evaporation concentrates brines favoring the precipitation of magnesium and/or sodium sulphates (mainly epsomite, hexahydrite, pentahydrite, starkeyite, konyaite, bloedite, mirabilite and thenardite) and halite minerals on the surface (Sanz-Montero et al., 2013a; Cabestrero et al., 2014b, 2016; Del Buey et al., 2016; Cabestrero et al., 2018). Along with the precipitation of sulphates and chlorides, clay authigenesis (up to 25% of clay minerals) also occurs (Cabestrero et al., 2014a).

3. Material and methods

3.1. Sample collection

For sedimentological and mineralogical analyses, up to 10 cm thick samples of sediment including a mineral layer and the overlying organic top of microbial mats were regularly collected between December 2009 and March 2017 in the three studied playa lakes. In addition, to analyze the bulk and clay mineralogical composition, a 30 cm thick profile of recently deposited microbial sediment was sampled from the top in LG lake in the 2nd of November of 2016 (Fig. 4). In the profile are represented most of the distinctive features of the microbial sediments accumulated through successive cycles of wet and drying (Fig. 3A). Two cores of lithified sediment, up to 35 cm in depth, were also obtained in AG in the 10th of June of 2013 (Fig. 5). The cores were collected in the shore (AG-S1-4; $39^\circ41'32.72''$, $-3^\circ18'8.87''$) and central part (AG-SB; $39^\circ41'35.66''$, $-3^\circ18'1.85''$) of the playa lake to evaluate the influence of location on the mineralogy. Other samples exhibiting distinctive and common sedimentary structures related with microbial mats were also collected. So, mat curls (MC-LG and MC-AG) and decaying mat portions (MF-LG) were sampled from LG and AG playas in March 2017 (Fig. 2A and B). Other type of sample showing vesicular structures (AC) was obtained in March 2016 from AC.

3.2. Water samples

Apart from sediment samples, water/brine samples were collected of each playa-lake, whenever it was possible. Water physicochemical parameters such as salinity (S), temperature (T), dissolved oxygen (DO), oxidation reduction potential (ORP), and pH values were recorded with a portable water multiparameter probe (Hanna Instruments 9828). The main cations and anions were analyzed by ion chromatography, using Dionex DX 500 ion and METROHM 940 Professional IC Vario chromatographs at CAI de Técnicas Geológicas (UCM).

3.3. Bulk and clay mineralogy (XRD)

About 50 samples were examined by random powder X-ray diffraction (XRD) analysis using a Bruker D8 Advance diffractometer with Cu K α radiation ($\lambda = 1.54060 \text{ \AA}$) and equipped with a Sol-X detector. The samples were scanned from 2 to $65^\circ 2\theta$ with a step size of $0.02^\circ 2\theta$ and a counting time of 0.5 s per step. XRD interpretation was based on the method described by Chung (1974) and using EVA Bruker software. For clay mineralogy, carbonates, sulphates and organic matter were removed from samples using 200 ml of 0.2 M HCl dissolution, continuously agitated for 20 min (Kübler, 1987; Nieto et al., 2016). $< 2 \mu\text{m}$ and $< 0.5 \mu\text{m}$ fractions of the treated sediment levels were separated using the centrifuge technique (Jackson, 1979). To obtain fractions below $2 \mu\text{m}$, cycles of 1000 rpm during 3 min were performed, whereas fractions below $0.5 \mu\text{m}$ were obtained by 2000 rpm during 10 min . Using Thermo Scientific Sorvall ST 16 Centrifuge. All size fractions were analyzed as oriented mounts prepared by smearing the slurries on glass slides. Three XRD diagrams were obtained for each size fraction: after air-drying (AD), ethylene-glycol (EG) and heating at 550°C at least 2 h . These samples were scanned from 2 to $35^\circ 2\theta$ with a step size of $0.02^\circ 2\theta$ and a counting time of 1 s per step. The quantification of the clay mineral assemblages was done by using the mineral intensity factor method (MIF) of Moore and Reynolds (1997).

3.4. Sedimentological textural features (SEM)

Textural features and mineral assemblages were established by scanning electron microscopy using images recorded with secondary and backscattered electrons, and energy dispersive X-ray systems (EDX). Freshly fractured surfaces of representative samples were air-dried and coated with Graphite and Au under vacuum conditions. SEM observations were performed using a FEI INSPECT microscope for environmental electron microscopy (ESEM), operating at 30 kV and high vacuum mode, and JSM 6335F (FEG-SEM) operating at 20 kV . Both models are equipped with an OXFORD INSTRUMENTS solid-state EDX detector.

3.5. Textural and crystallochemical features of Palygorskite-Sepiolite (TEM-AEM)

TEM observations and quantitative analyses, from eleven representative samples, were obtained from powdered portions prepared using C-coated Cu grids. The TEM data were obtained using two electron microscopes: the JEOL 3000F, operated at 300 kV , and the JEOL JEM 2100 microscope, operated at 200 kV . Quantitative analyses (AEM) of particles were obtained in STEM mode with an OXFORD INSTRUMENTS EDX microanalysis system in the first one.

4. Results

4.1. Hydrochemical and physicochemical parameters

Physical and chemical parameters of water column and pore waters for the period 2014–2017, are shown in Table 1. Analyses were done during diluted, mild and highly concentrated conditions in the three lakes AC, AG, LG. Following autumnal rain periods, the salinity values were consistently low (Table 1), being the lowest recorded: 3.05 gL^{-1} (AG); 11.71 gL^{-1} (AC); and 36.33 gL^{-1} (LG). Salinity kept rising as the lakes water evaporates reaching the maximum values of 13.97 gL^{-1} (AG); 55.09 gL^{-1} (AC); and 161.20 gL^{-1} (LG). The pH, DO and ORP varied strongly over time, ranging from 7.13 to 9.6 , from 0.0% to 203.9% and from -99.3 to 197.8 mV , respectively (Table 1).

Table 1
Hydrochemical and physicochemical features of the three-study plays-lakes. Data correspond to water samples taken from small marginal pools, the central lake, and interstitial pores.

	Date	Site	Air T	Water T	pH	DO	S	ORP	Cl ⁻	SO ₄ ²⁻	NO ₃ ⁻	CO ₃ ²⁻	HCO ₃ ⁻	Ca ²⁺	Mg ²⁺	Na ⁺	K ⁺
			°C	°C		%	g L ⁻¹	mV	mmol L ⁻¹	mmol L ⁻¹	mmol L ⁻¹	mmol L ⁻¹	mmol L ⁻¹	mmol L ⁻¹	mmol L ⁻¹	mmol L ⁻¹	mmol L ⁻¹
AC	May-14	Small pools	19.10	14.92	8.06	14.60	55.09	87.70	1374.39	1862.60	2.02	5.39	6.20	6.91	2030.96	1133.87	18.20
	Dec-14	Lake	6.60	6.42	8.72	68.90	11.71	162.22	160.45	64.68	-	-	-	14.30	77.20	122.84	3.15
	Dec-14	Pore water	-	-	-	-	-	-	263.27	99.70	-	-	-	14.75	134.85	181.18	5.73
	Jan-15	Lake	15.39	12.82	8.22	113.30	21.84	95.20	314.54	101.96	-	-	3.33	11.93	132.54	195.18	5.17
AG	Jan-15	Pore water	-	-	-	-	-	-	313.86	101.87	-	-	-	16.39	148.84	216.46	6.63
	Nov-14	Lake	11.69	13.38	8.75	17.80	3.05	197.80	4.79	15.30	0.05	-	0.72	8.13	6.95	6.53	0.58
	Nov-14	Pore water	-	-	-	-	-	-	128.08	164.18	0.55	-	-	12.15	97.57	138.03	10.65
	Dec-14	Lake	6.30	5.42	9.10	41.70	5.67	153.80	58.37	46.82	-	-	-	12.13	36.50	57.64	3.30
LG	Dec-14	Pore water	-	-	-	-	-	-	63.89	94.88	-	-	-	13.57	41.68	59.60	3.28
	Jan-15	Lake	13.67	11.80	9.04	64.80	13.97	-12.50	144.76	99.05	0.40	0.20	3.46	7.93	58.23	96.92	5.79
	Jan-15	Lake	11.13	19.45	9.60	203.90	36.33	28.60	425.07	183.25	-	1.48	4.02	5.14	144.97	260.91	17.02
	Mar-16	Pore water	-	-	-	-	-	-	4498.59	1898.95	-	-	47.41	9.58	1313.30	1558.00	100.51
	Nov-16	Lake	29.88	26.47	7.13	0.00	161.20	-99.30	2029.21	914.01	-	-	-	7.73	1156.64	712.01	83.20
	Nov-16	Pore water	-	-	-	-	-	-	1719.80	1414.51	-	-	-	< 25	1246.06	1635.47	88.22
	Mar-17	Lake	13.98	17.24	8.78	90.40	63.08	-23.20	85.13	448.13	-	0.28	8.97	13.87	303.85	571.59	66.94
	Mar-17	Pore water	-	-	-	-	-	-	774.65	485.62	-	-	-	14.67	564.99	684.43	47.03

4.2. Lake water and pore water variations in seasonal lakes

During autumn the dissolution of the evaporites precipitated in the previous dry season led to higher ionic concentrations in pore water than in the water column (AG, November 2014; Table 1). The first rains of the wet season also reactivated the drought-resistant microorganisms responsible for the decomposition of buried microbial mats (Fig. 3A), which accounted for higher contents of NO_3^- in the pore water than in the water column. The colder and drier stable conditions prevailing from November to December favored the ions exchange flux from the pore water, which resulted in a notable increase of ions content in the water column (Table 1, AC and AG). Despite that, the concentration of ions was still higher in the pore water, where the Mg^{2+} increased its ratio (Table 1, AG). In winter of 2015, the pore water and the water column showed a similar concentration of ions except for Mg^{2+} and Na^+ cations that remained slightly higher in the pore water (Table 1, AC).

4.3. Lake water variations in a permanent lake

LG lake has never dried out in the studied period, although it was in 2016 when it showed the highest variations (Table 1, LG). The relatively low concentration of ions in March 2016 resulted in a salinity of $36.33 \text{ g}\cdot\text{L}^{-1}$, and it increased to $161.20 \text{ g}\cdot\text{L}^{-1}$ after a dry summer. Between March and November 2016 physicochemical parameters varied widely mainly due to seasonal differences in microbial mats coverage and composition. In March 2016 and 2017 temperatures recorded in water were higher than in the air during March 2016 (19.45°C and 11.13°C) and March 2017 (17.24°C and 13.98°C), stimulating the growing of microbial mats (with abundant phototrophs), which accounted for high levels of oxygen production (203.9%), high pH values (9.6) and oxidizing conditions (26.6 mV). By contrast, in November, low pH (7.13) and DO (0%) values as well as reducing conditions (-99.3 mV) are explained by the lower temperature in water than in air and adverse environmental conditions including high salinity levels ($161.20 \text{ g}\cdot\text{L}^{-1}$) that led to the decayment of microbial mats, in which low production and/or very high oxygen consumption rates prevailed. Mg^{2+} and Na^+ are the most abundant cations, being more concentrated in pore waters ($1313.30 \text{ mmol}\cdot\text{L}^{-1}$ and $1558.00 \text{ mmol}\cdot\text{L}^{-1}$; respectively) than in open lake waters ($144.97 \text{ mmol}\cdot\text{L}^{-1}$ and $260.91 \text{ mmol}\cdot\text{L}^{-1}$; respectively). On the other hand, SO_4^{2-} and Cl^- are the dominant anions, being more concentrated in pore waters ($1898.95 \text{ mmol}\cdot\text{L}^{-1}$ and $4498.59 \text{ mmol}\cdot\text{L}^{-1}$; respectively) than in open lake ($183.25 \text{ mmol}\cdot\text{L}^{-1}$ and $425.07 \text{ mmol}\cdot\text{L}^{-1}$; respectively). The biggest difference in concentration of ions between open lake and pore waters was recorded in March 2016.

4.4. Dissolved silicon variations

Silicon dissolved in water was very low in AC and AG lakes, oscillating from 0.06 to $0.2 \mu\text{g}\cdot\text{mL}^{-1}$ (Table 2). In the shore of LG the contents of silicon (Si) were slightly higher and varied in the range of < 0.04 to $6.6 \mu\text{g}\cdot\text{mL}^{-1}$. The lowest value coincided with the lowest pH found (7.13) and a very high salinity ($161.2 \text{ g}\cdot\text{L}^{-1}$). On the contrary, the highest Si content was concomitant with a relatively low salinity ($47.5 \text{ g}\cdot\text{L}^{-1}$) and the highest pH ever recorded (10.26). As the pH, the Si values increase towards the center of LG. The concentration of Si in pore water (up to $11.80 \mu\text{g}\cdot\text{mL}^{-1}$) is invariably much higher than in lake water (Table 2).

4.5. Sedimentological and bulk mineralogical characterization

4.5.1. Surficial microbial sediments

Microbial mats that proliferate on the bed are disrupted after stormy or desiccation events (Sanz-Montero and Rodríguez-Aranda, 2013), producing mat fragments with uplifted margins detached from the layer

Table 2

Si concentration, salinity (S) and pH values from different playa lake spots.

Lake	Date	Spot	Si ($\mu\text{g}\cdot\text{mL}^{-1}$)	S ($\text{g}\cdot\text{L}^{-1}$)	pH
AG	25/04/2013	Shore	0.07	11.27	9.16
AG	28/01/2014	Shore	0.10	5.67	9.10
AG	10/02/2014	Centre	0.10	4.90	8.58
AC	26/04/2013	Shore	0.06	18.79	9.20
AC	04/01/2014	Shore	0.20	11.06	8.11
AC	28/01/2014	Shore	0.10	11.71	8.72
AC	10/02/2014	Shore	0.10	10.16	8.84
LG	28/01/2014	Shore	6.60	47.54	10.26
LG	10/02/2014	Shore	4.40	48.26	9.23
LG	02/11/2016	Shore	< 0.04	161.20	7.13
LG	02/11/2016	Pore water	8.10	–	–
LG	11/11/2016	Shore	2.50	48.97	8.78
LG	11/11/2016	Centre	2.80	45.90	9.06
LG	14/03/2017	Shore	0.25	63.08	8.78
LG	14/03/2017	Centre	1.30	63.70	8.99
LG	14/03/2017	Pore water	11.80	–	–

underneath (mat curls) (Fig. 2A and B). Two types of mat curls were analyzed. One type forms by desiccation of the organic portions (MC-LG and MC-AG) (Fig. 2A). The second type consists of wet and incipiently decayed microbial mat portions (MF-LG) transported to the water's edge by currents (Fig. 2B). Other typical surficial feature of microbial mats is the vesicular structures (AC) that are commonly produced by gas bubbles trapped within the sediment, especially after flooding events.

Bulk mineralogical composition of the mat curls (Fig. 2A) and wet and incipiently decayed microbial mat portions (MF-LG; Fig. 2B) reveals that they contain high proportion of phyllosilicates (about 30%) and gypsum $\text{CaSO}_4\cdot 2\text{H}_2\text{O}$ (25–35%), while the silt-sized quartz and feldspars grains together represent up to 25% of the total (Table 3). Other sulphate, hexahydrate $\text{MgSO}_4\cdot 6\text{H}_2\text{O}$, is only present in the LG mat portions (Fig. 2B). By contrast, the proportion of the carbonate minerals, calcite and dolomite, in AG (18%) is double than LG. With some differences, mainly concerning to the amount of phyllosilicates that hardly account for the 15%, the mineralogy of the incipiently decayed microbial mat portions and sediments with vesicular structures (AC) is similar to that of the dry mat curls (Fig. 2A).

4.5.2. Longar profile

The sediment of LG profile is an irregularly layered silty mud with variable amounts of evaporites and organic compounds that are responsible for the different colorations exhibited, ranging from white to black with localized green, red and purple pigmentations (Figs. 3 and 4). Five distinctive layers a few cm in thickness are differentiated downwards from the puffy surface (Fig. 4). The uppermost layer consists of wavy laminated microbial deposits with alternation of lithified and non-lithified laminae. In some parts the vertical lamination of the microbial community is still visible by the distinctive green, red, and purple colorations (Fig. 3A). The underlying is a patchily lithified black layer with gas scape pores that can extend to the surface. The black layer overlies gray to white multilaminated deposits. Below, two burrowed evaporitic layers are visible (Fig. 3B and C). The burrows are arranged in all directions displaying a tangle pattern. This type of burrowing is produced by feeding of the *Ephydra* (shore flies) on microbial mats just on the shoreline where they proliferate (Sanz-Montero et al., 2013a). The deepest, is a buried black layer crowded with a complex network of irregular burrows which enhanced the oxidation of the reduced sediment around them (Fig. 3D). These burrows are digged by beetles (*Bloedius*) on moist and microbial mat covered surfaces (Sanz-Montero et al., 2013a; Rodríguez-Aranda et al., 2014).

The sediment is comprised of a mixture of authigenic and detrital mineral assemblages that include sulphates, chlorides, carbonates and silicates, and show some variations along the profile (Fig. 4B and

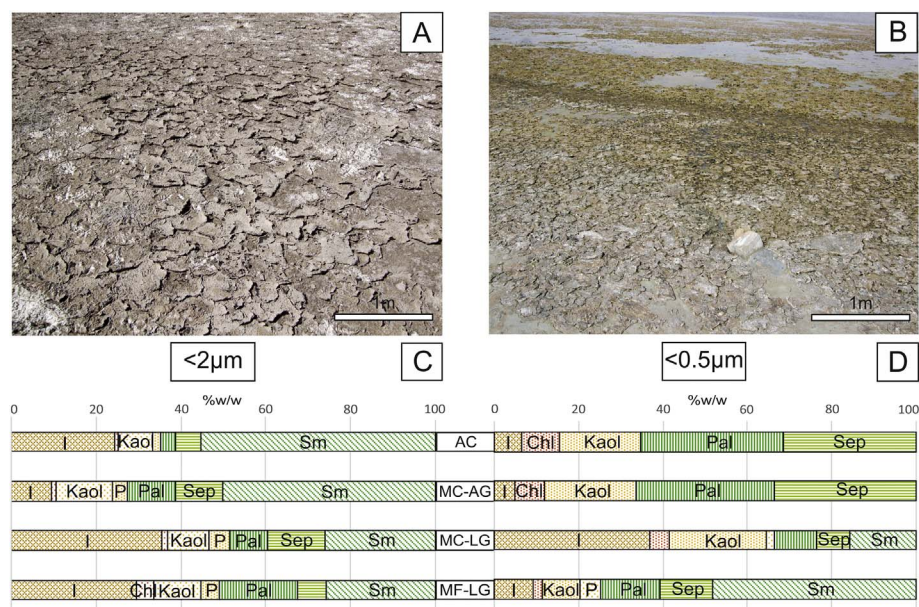


Fig. 2. Surfacial microbial sedimentary structures and clay mineral assemblages of mat curls (MC-AG and MC-LG), microbial mat portions (MF-LG) and sediment with vesicular pores (AC). A: Mat curls on the shores of AG. B: Decaying mat portions on the shore of LG C: Clay mineralogy fraction (< 2µm) D: Clay mineralogy fraction (< 0.5µm) I: illite, Chl: chlorite, Kaol: kaolinite, Prl: pyrophyllite, Pal: palygorskite, Sep: sepiolite, Sm: smectite.

Table 3). Gypsum $\text{CaSO}_4 \cdot 2\text{H}_2\text{O}$, with proportions ranging between 40 and 55%, is the most abundant authigenic mineral followed by hexahydrate $\text{MgSO}_4 \cdot 6\text{H}_2\text{O}$, which reaches its maximum value (30%) in the bioturbated evaporitic layer. Other hydrated- magnesium sulphates, epsomite $\text{MgSO}_4 \cdot 7\text{H}_2\text{O}$ and starkeyite $\text{MgSO}_4 \cdot 4\text{H}_2\text{O}$, are locally present, too. Small amounts of starkeyite occur associated with hexahydrate at the deepest bioturbated layer, whilst epsomite makes up 15% of the multilaminated layer. Minor halite is ubiquitous thorough. The carbonates, calcite CaCO_3 , its polymorph aragonite together with dolomite $\text{CaMg}(\text{CO}_3)_2$ account for < 10% of the total mineralogical composition of the deposit. Calcite and dolomite remain constant throughout, whereas minor aragonite is restricted to the topmost layer of the profile

(**Table 3**). Up to 10% of silt-sized detrital silicates, quartz and feldspar, remain nearly constant down the profile. By contrast, the clay mineral contents vary in the range of 10% to 20% (**Fig. 4B** and **Table 3**).

4.5.3. Altillo Grande (AG) profiles

The two cores, collected from the shore (**Fig. 5A**) and in the inner part (**Fig. 5C**) of AG, are composed of a mixture of silty mud and whitish evaporites. The structure of the sediment is massive with common bioturbation traces. They consist of four to five gross bands separated by diffuse and irregular contacts and mostly defined by gradual to abrupt variations in the relative abundance of evaporites. The uppermost 20 cm of both profiles are characterized by the profusion of pores,

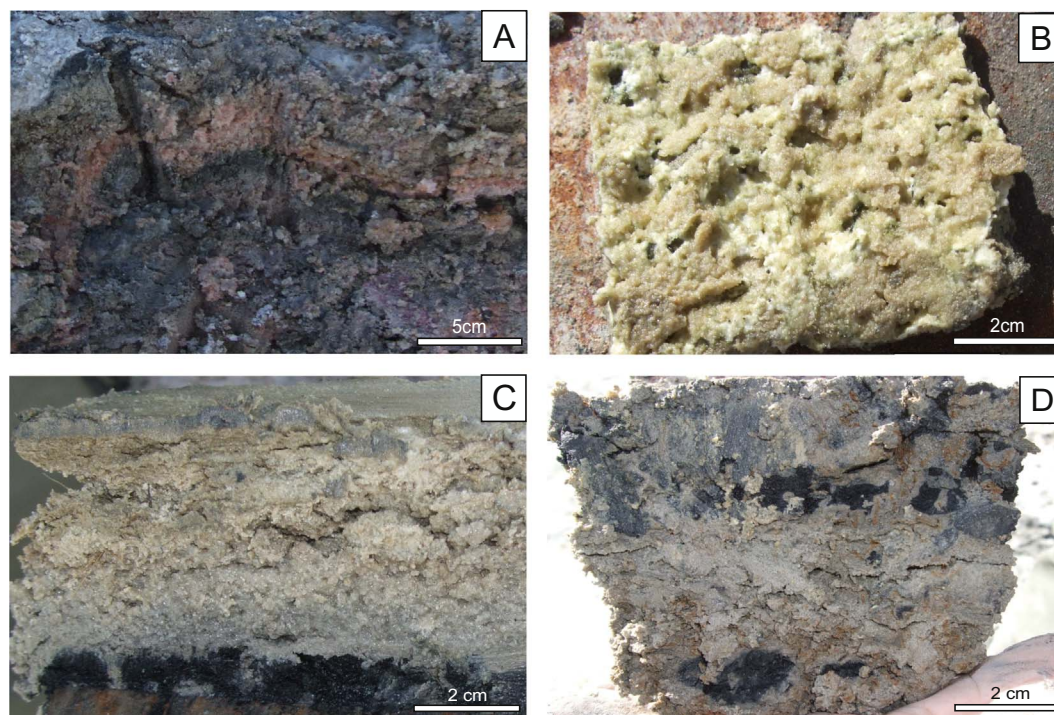


Fig. 3. Sedimentary layers found through the sedimentary profile excavated at the shore of LG (see **Fig. 4**). A: Surfacial microbial mat with vertical lamination showing green, red, and purple colorations. B: Burrowed evaporitic layer (LG-5) C: Detail of a burrowed evaporitic layer (LG-5b). D: Deepest black layer at the bottom of the trench with irregular burrows highlighted by oxidized sediment (LG-6). (For interpretation of the references to color in this figure legend, the reader is referred to the web version of this article.)

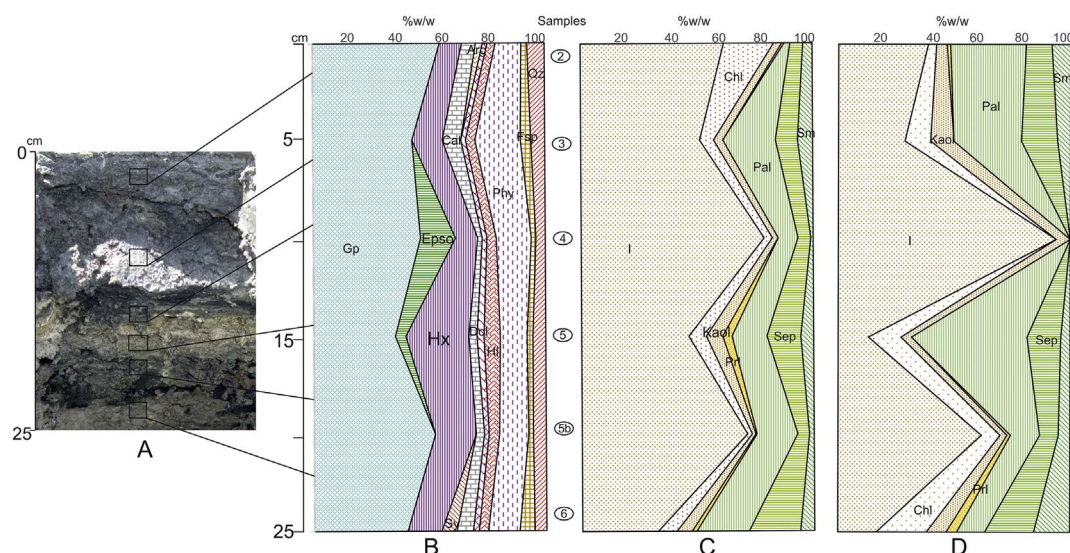


Fig. 4. A: Trench through the recently deposited sediment in the water edge of LG. Squares indicate the location of samples LG-2 to LG-6 from top to bottom. B: Bulk mineral composition along the profile. Mineralogy of the < 2 μm fraction (C) and < 0.5 μm fraction (D). Gp: gypsum, Epso: epsomite, Hx: hexahydrite, Sy: starkeyite, Arg: aragonite, Cal: calcite, Dol: dolomite, Hl: halite, Phy: phyllosilicates, Fsp: feldspar, Qz: quartz.

up to 3 mm in diameter that can be connected vertically through channel-like pores. This porosity is reduced in depth. Gravel sized detrital fragments occur floating in the mud both in the uppermost layer and scattered through the outer core. An indurated bed is forming the base of the two profiles. The mineralogical bulk composition of the two cores consists basically of a mix of sulphates, silicates, carbonates and low amounts of chlorides (chiefly halite and locally carnallite $\text{KMgCl}_3 \cdot 6\text{H}_2\text{O}$ in the shore deposits) although there are differences between them in the relative proportions of the main groups of minerals (Fig. 5A and C). The most abundant minerals, comprising up to 50% of the total, are gypsum and phyllosilicates in the outer and inner cores, respectively (Table 3). The percentages of both vary significantly along the two profiles. In fact, an inverse trend between gypsum and phyllosilicates is observed in the two cases (Table 3). Except for the most soluble evaporites (chlorides, bloedite), the remaining minerals vary in a narrow range (Fig. 5A and C).

4.6. Microfabrics of the microbial sediment

The microfabrics of the microbial sediments have been examined by different microscopy techniques to determine the textural relationships between the main minerals and the microorganisms (Fig. 6). In optical microscopy the active microbial mats exhibit a variety of intergradational fabrics dominated by a filamentous microfabric that reflect cyanobacterial layering (Fig. 6A). The dark organic cyanobacterial filaments grade laterally to degraded areas of the microbial mat that show a massive microfabric, within which some organic laminae are vaguely recognizable. Under higher magnification, it is clearly visible that minute and poorly crystalline clays occur within the degraded parts (Fig. 6B) associated to gypsum microcrystals. The inner lamination is also disrupted by burrows infilled with lenticular gypsum. This type of cylindrical and meniscate burrows are caused by ephyridia larvae (Sanz-Montero et al., 2013a).

In active microbial mats, the dominant microorganisms (cyanobacteria and diatoms) have the ability of trapping and binding the detrital particles in the EPS they produce (Fig. 6A–C). The detrital components (chiefly, quartz, feldspars and mica/illite) appear extensively dissolved and disaggregated as a result of interaction between the microbes and minerals (Fig. 6C and D). Together with the detrital grains, authigenic gypsum and carbonate crystals often occur in the organomineral matrix (Fig. 6D and E). So upon degradation of the matrix, the gypsum crystals appear embedded by organomineral clots

(Fig. 6B) that contain variable amounts of Si, Al, Mg, Fe, etc. (Fig. 6E) derived from the altered silicates lying in the vicinity (Fig. 6C and D). More detailed observations by FE-SEM demonstrate that sometimes gypsum crystals are covered by irregular to fiber-shaped aggregates exhibiting incipient crystalline faces composed of Si, Al and Mg (Fig. 6F).

4.7. Clay mineralogy

4.7.1. Mineralogy and distribution of clay minerals

The results of clay mineralogical analyses by XRD conducted on all the variety of microbial sediment are represented in Table 4 and Figs. 2C and D, 4, 5 and 7. The clay minerals detected are: illite (I), representing between 5%–90% of the phyllosilicates, sepiolite (Sep), 0%–90%, smectites (Sm), 0%–55%, palygorskite (Pal), 0%–50%, kaolinite (Kaol), 1%–30%, chlorite (Chl), 0%–20%, pyrophyllite (Prl), 0%–5%. According to the chemical composition and order degree (Fig. 7), two groups of clays have been differentiated: the first is comprised of I-Kaol-Chl-Prl and the second embraces the remaining Mg-rich clays that on average constitute about 50% of the phyllosilicates, although its spatial and vertical distribution is variable. Parallely, statistical analysis reveals that the concentration of the two groups vary inversely having a correlation coefficient $R^2 = 1$ (Fig. 4C and D, Figs. 1S and 8S).

The assemblage comprised of I-Kaol-Chl-Prl is ubiquitous in all surficial and buried sediment and are recognizable by sharp reflections in the diffractograms (Fig. 7). In the Mg-rich group, Pal and Sep occur associated in most of analyzed samples, unlike Sm that appear discontinuously in AG (Fig. 5B and D). Smectites are only recognized after ethylene-glycol solvation (EG) by the shift of the 001 reflection to the range 17.0–18.7 Å (Fig. 7). All the magnesian phases are characterized by broad reflections (Fig. 7 and Fig. 12S), indicative of their small size and/or low order. The concentrations of the clays by size follow different trends in the < 2 μm and < 0.5 μm fractions (Figs. 2 and 4 and Table 4). I, which is predominant in the < 2 μm fraction, decreases significantly in the < 0.5 μm fraction. In general, Sep and Pal exhibit similar behavior and tend to accumulate in the smaller fraction (< 0.5 μm). This increase is more prominent, especially for Pal, where the phyllosilicates occur in high amounts (about 65%), as is the case of some surficial samples and in a buried bioturbated layer of LG (Fig. 4D). By contrast, the Sep-Pal group occurs with low contents in the < 2 μm fraction and practically disappears in the < 0.5 μm fraction, just in the epsomite-bearing layer of the LG profile (Fig. 4B–D and Table 4).

Table 3

Bulk mineralogy: semi quantification results obtained by XRD powder method of recent and buried microbial sediment from LG, AG and AC playa-lakes. With the exception of Phy, Phyllosilicates; Hx, Hexahedryte; Epso, epsomite; Sy, starkeyite; Blo, bloedite; and Cn, carnallite abbreviations are according to [Whitney and Evans \(2010\)](#). Gp, Gypsum; Cal, Calcite; Dol, Dolomite; Hl, Halite; Qz, Quartz; and Fsp, Feldspar. (-) Not detected.

Sample	Location/type	Gp	Hx	Epso	Sy	Blo	Cal	Arg	Dol	Hl	Cn	Qz	Fsp	Phy
		%w/w	%w/w	%w/w	%w/w	%w/w	%w/w	%w/w	%w/w	%w/w	%w/w	%w/w	%w/w	%w/w
LG-2	Shore trench	55	10	-	-	-	6	3	2	3	-	3	8	11
LG-3	Shore trench	43	13	-	-	-	8	-	2	4	-	5	6	19
LG-4	Shore trench	47	10	15	-	-	2	-	2	4	-	2	4	15
LG-5	Shore trench	35	27	5	-	-	3	-	3	7	-	3	6	11
LG-5b	Shore trench	53	18	-	-	-	3	-	2	5	-	2	5	12
LG-6	Shore trench	41	15	-	6	-	7	-	3	4	-	6	5	14
MC-LG	Surficial mat curls	35	10	-	-	-	8	-	-	-	-	6	8	31
MF-LG	Surficial decaying mat	30	22	-	-	-	6	-	-	6	-	4	14	16
AG S1 0-2	Shore core	38	4	-	-	3	11	-	-	1	-	16	6	12
AG S1 2-4	Shore core	32	5	-	-	4	7	-	-	1	4	13	5	22
AG S1 4-6	Shore core	32	-	-	-	6	20	-	-	2	-	14	7	20
AG S1 6-8	Shore core	38	-	-	-	5	8	-	-	1	-	24	6	18
AG S1 8-10	Shore core	44	-	-	-	-	7	-	-	2	-	20	7	21
AG S1 10-12	Shore core	53	-	-	-	3	5	-	-	1	-	9	5	23
AG S1 12-15	Shore core	43	-	-	-	3	5	-	-	1	-	6	6	28
AG S2 0-2	Shore core	57	-	-	-	4	5	-	-	1	-	8	5	20
AG S2 2-4	Shore core	52	-	-	-	2	7	-	-	1	-	24	3	11
AG S2 4-6	Shore core	52	-	-	-	-	8	-	-	1	-	21	5	13
AG S2 6-8	Shore core	39	-	-	-	-	10	-	-	1	-	15	8	27
AG S3 0-2	Shore core	25	4	-	-	6	9	-	-	2	3	15	9	22
AG S3 2-4	Shore core	22	-	-	-	7	10	-	-	2	-	22	11	27
AG S3 4-6	Shore core	27	-	-	-	9	9	-	-	2	-	13	8	32
AG S3 6-8	Shore core	59	-	-	-	-	5	-	-	1	-	11	6	17
AG S3 8-10	Shore core	64	-	-	-	2	3	-	-	1	-	5	7	18
AG S3 10-13	Shore core	63	-	-	-	-	2	-	-	2	-	4	8	21
AG S4 0-2	Shore core	77	-	-	-	-	1	-	-	1	-	2	6	14
AG S4 2-5	Shore core	71	-	-	-	-	2	-	-	2	-	3	7	16
AG SB 0-2	Inner core	17	-	-	-	10	13	-	-	2	-	10	10	39
AG SB 2-4	Inner core	22	-	-	-	5	13	-	-	3	-	7	10	41
AG SB 4-6	Inner core	22	-	-	-	6	14	-	-	2	-	7	14	36
AG SB 6-8	Inner core	33	-	-	-	5	7	-	-	1	-	6	11	37
AG SB 8-10	Inner core	39	-	-	-	5	7	-	-	1	-	6	8	34
AG SB 10-12	Inner core	37	-	-	-	5	7	-	-	1	-	5	7	38
AG SB 12-14	Inner core	37	-	-	-	-	9	-	-	1	-	8	8	38
AG SB 14-16	Inner core	29	-	-	-	-	3	-	-	1	-	6	11	50
AG SB 16-18	Inner core	41	-	-	-	-	9	-	-	-	-	8	-	43
AG SB 18-20	Inner core	29	-	-	-	6	5	-	-	-	-	8	11	41
AG SB 20-22	Inner core	31	-	-	-	5	2	-	-	1	-	5	8	47
AG SB 22-24	Inner core	33	-	-	-	5	2	-	-	-	-	7	10	44
AG SB 24-26	Inner core	39	-	-	-	5	2	-	-	-	-	8	8	38
AG SB 26-28	Inner core	31	-	-	-	6	1	-	-	1	-	12	11	39
AG SB 28-30	Inner core	49	-	-	-	4	-	-	-	1	-	8	5	33
AG SB 30-32	Inner core	47	-	-	-	5	4	-	5	1	-	5	8	26
AG SB 32-34	Inner core	32	-	-	-	5	7	-	7	2	-	2	8	37
MC-AG	Surficial mat curls	23	-	-	-	-	18	-	2	5	-	16	10	29
ALTC	Surficial porous sediment	29	-	-	-	-	27	-	-	-	-	17	10	14

Distinctly, Sep is more abundant than Pal and increases with depth on the shore of AG (Fig. 5B and Table 4).

4.7.2. Textural features

The overall textural and microtextural analyses by TEM of Pal-Sep clays confirm that the fibers are nanometer-sized and poorly ordered (Fig. 8). The incipient crystals present a low degree of aggregation according to the classification done by [García-Romero and Suárez \(2014\)](#).

In the recently deposited sediment of LG, the crystals commonly occur as lath and rod-shaped fibers of Pal and Sep with width (W)/length (L) ratios ranging 0.1–0.4, varying the L and W of the individual crystals: 100 nm–400 nm and 9.70 nm–75 nm, respectively (Fig. 8A and B). In addition, up to 1.5 µm long and 200 nm wide bundles, composed of several rods arranged in parallel to the c-axis of the fiber, are only found in the deepest layer of the profile.

In the more lithified deposits of AG, the bundles of Sep are bigger, 800 nm to 2.5 µm in L (Fig. 8C) and are predominant in bioturbated layers (Fig. 5). Two types of bundles are identifiable with W/L ratios varying 0.13 to 0.3. One of the types is comprised of fibers shorter than

1 µm that grew tightly connected to each other forming a dense mesh. In the second type of bundles, the fibers, 1–10 µm in L, grow forming open to close aggregates. Besides, individual lath and rod-shaped crystals, characterized by W/L from 0.04 to 0.5, are common in different layers of the profiles.

In general, the laths and rods forms are straight and rigid but the bundles tend to be curled (Fig. 8A–C). It is notorious that Pal laths and rods are in direct contact with the EPS matrix (Fig. 8D), confirming SEM observations (Fig. 6E). In fact, rod shaped fibers project outwards from the EPS (Fig. 8D and G), on occasions forming bridges between shrunk masses of EPS (Fig. 8H) that progressively separate as the EPS undergo retraction by dehydration (Fig. 8G). More hydrated EPS show a 3D alveolar morphology (Fig. 8D, G and H) and contain very high amounts of Mg accompanied by variable Si, S, Al, Fe, Cl, K, Na (Fig. 8F) and P. The components of the dehydrated EPS are similar but the relative contents of Mg and O are much lower in comparison with the hydrated counterparts (Fig. 8H). The lower amounts of ions attached to dehydrated EPS (Fig. 8I) with respect to the hydrated masses (Fig. 8K) is related with the lower amount of charge present in the degraded EPS.

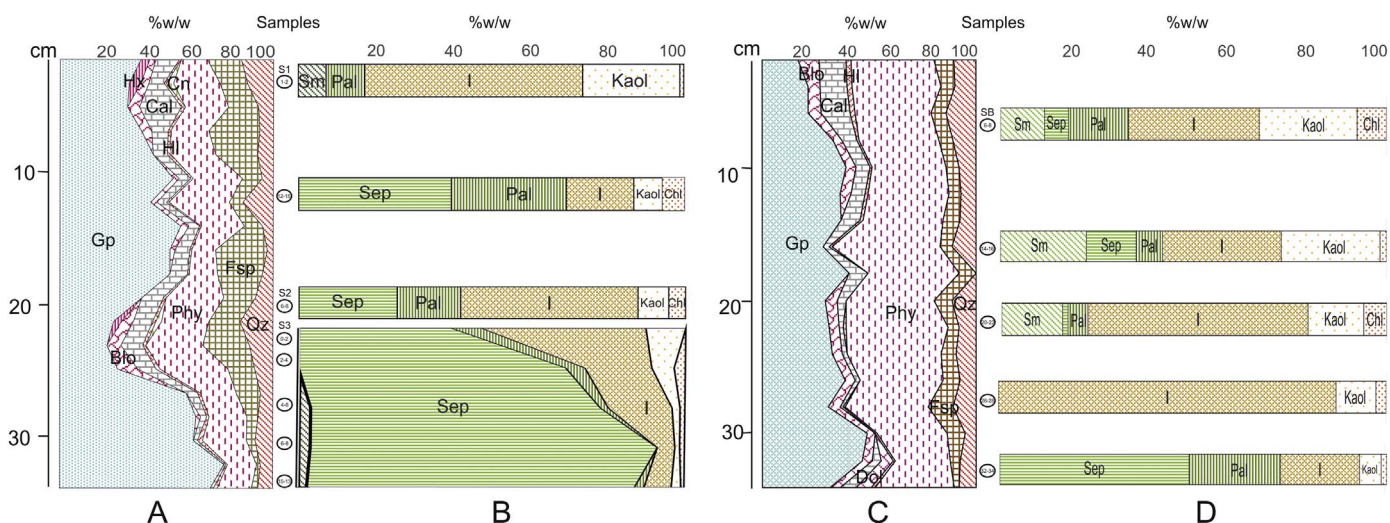


Fig. 5. Mineralogical composition of two cores taken from the shore and the center of AG. A: Shore core, bulk mineralogy. B: Clay mineral assemblages (< 2 μm) in the shore of AG. C: Bulk mineralogy of the inner core. D: Clay mineral assemblages (< 2 μm) in the inner core of AG.

Structurally, the degraded EPS are also different, exhibiting a collapsed and massive structure. Some fibers act as an intermediate and continuum phase between the turgent to collapsed state transition (Fig. 8H). These fibers typically contain prominent Si as well as Mg, Al and Fe (Fig. 8J), which fits well with a Pal composition. The presence of randomly-oriented fibers of Pal along with other amorphous or poorly ordered phases within the EPS (Fig. 8D, G and H), is coherent with their polycrystalline condition (Fig. 8G).

4.7.3. Crystallochemical composition

The overall analysis of the Pal-Sep clays by TEM-AEM (Fig. 9) reveals that there is a vast variability in the chemical composition of the group as all intermediate phases between pure Pal and pure Sep have been determined (Suárez and García-Romero, 2011).

Compositionally, the clays present in the dark layer of LG (LG-3) are scattered through most of the fields of the diagram. This contrasts with the well-defined composition of the underlying layers, LG-5 and LG-6, that mostly contain Mg-Pal ($[\text{Si}_{12}\text{O}_{30}\text{Mg}_8(\text{OH})_4(\text{OH}_2)_2]_{0.6}[\text{Si}_8\text{O}_{20}(\text{Mg}_2\text{Fe}_2)_{0.6}(\text{Mg}_2\text{Al}_2)_{0.4}(\text{OH})_2(\text{OH}_2)_2]_{0.4}n\text{H}_2\text{O}$) and a mixture of pure and common Pal ($[\text{Si}_{12}\text{O}_{30}\text{Mg}_8(\text{OH})_4(\text{OH}_2)_2]_{0.6}[\text{Si}_8\text{O}_{20}(\text{Mg}_2\text{Fe}_2)_{0.25}(\text{Mg}_2\text{Al}_2)_{0.75}(\text{OH})_2(\text{OH}_2)_2]_{0.4}n\text{H}_2\text{O}$) (Suárez and García-Romero, 2013). Pal belonging to the mat curls (MC-LG) and decaying mat portions (MF-LG) have chemical intermediate compositions between LG-6 and LG-5.

A remarkable spatial and vertical variability is observed in the more lithified sediment of AG. In the inner core, some layers (AG SB 14–16) contain average Fe_2O_3 values (0.48%–8.22% Fe_2O_3) but other shallower layer (AG SB 6–8) are extremely shifted to higher Fe_2O_3 contents (6.71% to 16.92%). In the marginal core (AG S3 2–4 and AG S3 6–8), the clays are characterized by high MgO contents (9.20%–20.52%) and the variability of Fe_2O_3 that range from negligible in one layer to be highly variable in the underlying (0.76%–3.91%). The chemical composition of the first corresponds to a pure Sep (15.32% MgO, 0% Al_2O_3 , 0% Fe_2O_3). By contrast, the clays of the mat curls distributed over the surface of LG host a chemical composition that fits to pure-common Pal ($[\text{Si}_{12}\text{O}_{30}\text{Mg}_8(\text{OH})_4(\text{OH}_2)_2]_{0.2}[\text{Si}_8\text{O}_{20}(\text{Mg}_2\text{Fe}_2)_{0.35}(\text{Mg}_2\text{Al}_2)_{0.65}(\text{OH})_2(\text{OH}_2)_2]_{0.8}n\text{H}_2\text{O}$) (Suárez and García-Romero, 2013). The remaining surface samples from AC are chemically heterogeneous, varying widely in MgO values (9.55% to 18.41%) and shortly in Fe_2O_3 contents (1.60%–3.73%).

5. Discussion

The previous results provide evidence for the extensive formation of Pal-Sep clays in modern lacustrine environment and shed light on the

conditions of formation of these minerals that have remained elusive for years. Sedimentological, mineralogical and microscopical determinations show that the widespread formation of the Mg-rich clays occurs in microenvironments within the matrix of the microbial mats (EPS), which argues in favor of a biochemical origin for this group of minerals.

5.1. Authigenic formation of Mg-rich phyllosilicates

A number of signatures (distribution patterns and associations, mineral assemblages as well as textural and chemical features) provide criteria for interpreting the Mg-rich phyllosilicates, particularly the more abundant Pal-Sep group, as authigenic rather than detrital in origin.

The Mg-clays were formed in the microbial mats as unequivocally reflects the close association observed at all scales between them. Specifically, transmission electron microscopy provides compelling evidence for the crystallization of the fibrous silicates on the EPS of microbial mats (Fig. 8H). In addition, we found an opposite distribution pattern of the clay mineral assemblages throughout the microbial sediment. The detrital clay group (I, Chl, Kaol and Prl), commonly exhibiting destruction marks, is dominant in surficial, growing microbial mats. In contrast, the Mg-clays become more abundant in the decaying and buried microbial mats. This divergent trend is statistically confirmed by a perfect negative correlation between the two assemblages of clays and reveals different mechanisms of formation for each type (Figs. 1SA and B, 8S).

The full Mg-clay paragenesis, in addition to Sep and Pal, locally includes variable amounts of Sm. The composition of this paragenesis by itself denotes the authigenicity of the fibrous clays as it includes the main groups of neoformed clays reported in ancient lacustrine basins (Jones and Galan, 1988; Calvo et al., 1999; Meunier, 2005; Galán and Pozo, 2011). As in the study cases, where Mg is the dominant cation in the water, ancient Mg-phyllosilicates formed in hydrologically closed basins with Mg-enriched waters (Calvo et al., 1999; Calvo and Pozo, 2013; Jones and Deocampo, 2003). The results of the present study further confirm that interstitial water of these evaporitic basins systematically contains more Mg and Si than the surface water (Tables 1 and 2). The physicochemical changes in the pore water are chiefly promoted by microbial metabolisms that control the production or consumption of oxygen, the redox reactions, the release of gases, etc. These changes have an impact on pH (Cabestrero and Sanz-Montero, 2018) that is known to control the Mg-clay system along with the Mg and Si contents (Tosca and Masterson, 2014). Accordingly, the ionic supply of Si from the destruction of detrital grains in the microbial mats proved crucial for clay authigenesis in the study playa lakes where the silica dissolved in the surficial water is negligible. Significant higher

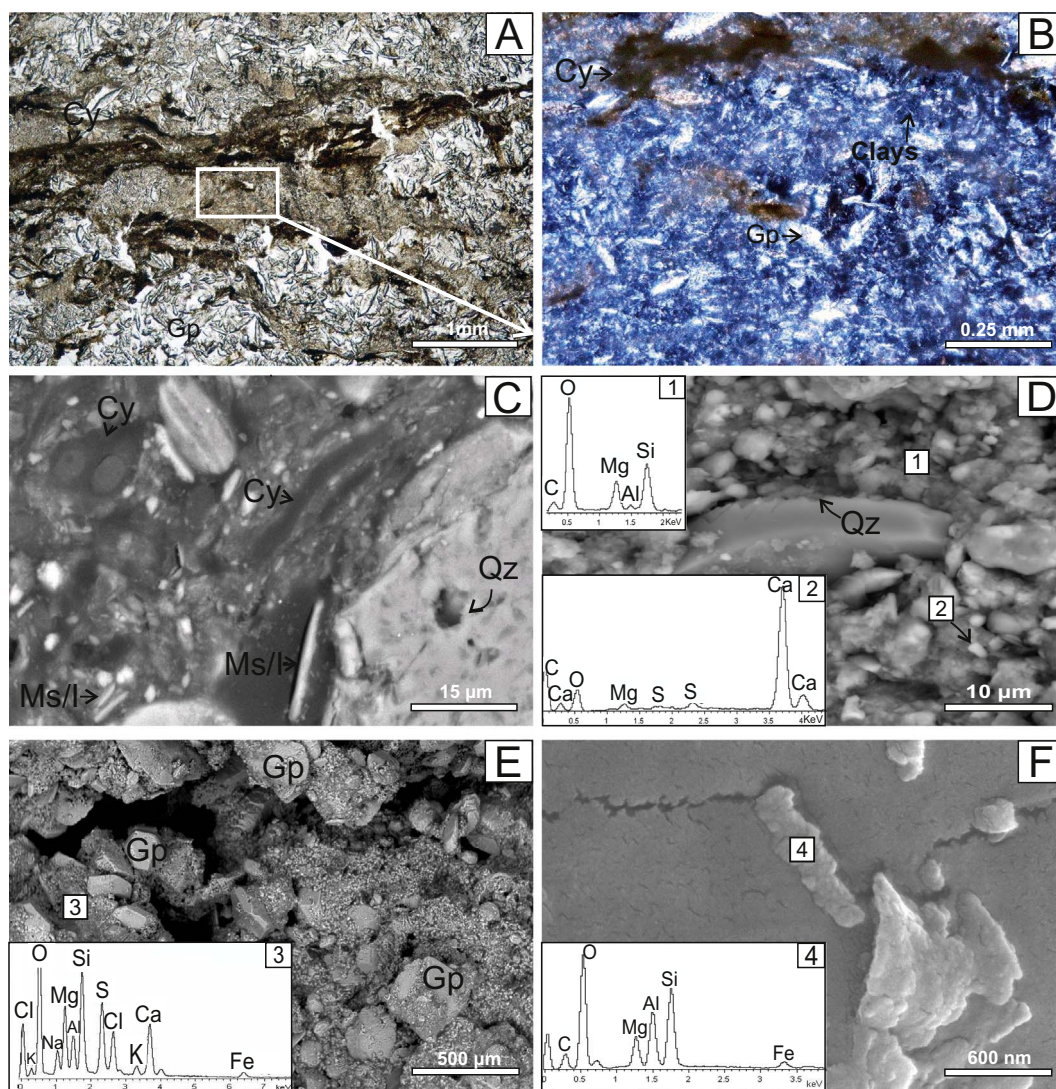


Fig. 6. Light and electron microscopy images showing the micro and ultrafabrics of the microbial sediments. A: Parallel polar microphotograph of active microbial mat showing microbial mat layers disrupted by burrows infilled with lenticular gypsum. The laminar microfabric, defined by dark organic filaments of cyanobacteria (Cy), gradually pass to degraded areas with some filament remains (see magnified square area in B). B: Minute and poorly crystalline clays have precipitated within the massive degraded area (squared in A), where some organic filamentous are still visible. Notice gypsum microcrystals (Gp) precipitated within the filaments. C: Secondary electron image of Quartz (Qz), mica/illite (Ms/I) and other detrital grains trapped in the EPS produced by cyanobacteria (Cy). Notice the degradation marks in quartz (Qz). D: Secondary electron image of a detrital quartz grain (Qz) surrounded by a mixture of carbonates (2) and Mg-clay minerals (1). E: Secondary electron image showing gypsum crystals (Gp) embedded in the organomineral matrix (3) of the microbial mats. F: FEG-SEM microphotograph (backscattered electron mode) of a gypsum crystal (Gp) covered by irregular to fiber-shaped aggregates (4) exhibiting incipient crystalline faces.

values of Si dissolved in pore water than in surficial water further support that the Si reservoir is in the more labile detrital grains. A similar argument may apply for explaining the source of Al.

Characterized by broad diffraction reflections, the fibrous phyllosilicates are poorly ordered and nanometer-sized phases (the majority are $< 0.5 \mu\text{m}$). These textural properties are typical of authigenic and biogenic clays reported by Konhauser et al. (1993). The Pal-Sep crystals occur in the three different stages of aggregation described by García-Romero and Suárez (2013): laths, rods and bundles. The laths are the smallest, stable and identifiable units (Fig. 8G), and they, in turn, result from the aggregation of much smaller particles “nanolaths”, which is consistent with their crystallization in situ. The aggregation of laths, parallel to the c-axis results in wider laths and rods (García-Romero and Suárez, 2014). The two types of Sep bundles observed can be the result of two different crystal growth processes. Assuming that the growth system is far from equilibrium (Cölfen and Antonietti, 2008), an oriented attachment mechanism is proposed for bundles shorter than $1 \mu\text{m}$ that grew tightly connected to each other forming a dense mesh. By contrast, the second type of bundles, $1\text{--}10 \mu\text{m}$ in length that form open to close

aggregates (Fig. 8C), are thought to have grown in conditions close to the equilibrium (García-Romero and Suárez, 2014).

The lower (Mg + Si): Al ratios measured in the Pal laths in comparison with the larger and more aggregated crystals (rods and sepiolitic bundles) is a chemical trend that was also observed by Tazaki (1997) during the mineralization of layer silicates around microbial cells and demonstrates that the fibers grow in successive stages. The compositional changes in the fluids explain the formation of all intermediate phases in the entire Pal-Sep polysomatic series, including an uncommon Fe-rich phase in AG (Fig. 9). It is not coincidental that such ferrous mineral formed in a sedimentary bed where detrital chlorite abounds (Fig. 5D) as it was shown that the destruction of chlorite releases Fe which is incorporated in the minerals forming in its vicinity (Sanz-Montero et al., 2009b). Except for the Fe-rich type, the compositional variability observed in the neoformed clays was also typical of the fossil clayey counterparts (García-Romero et al., 2004).

The occurrence of the Mg-rich clays in all the studied samples, ranging from recently formed to lithified microbial sediments, reveal that clay crystallization occurs on the surface and starts as soon as the

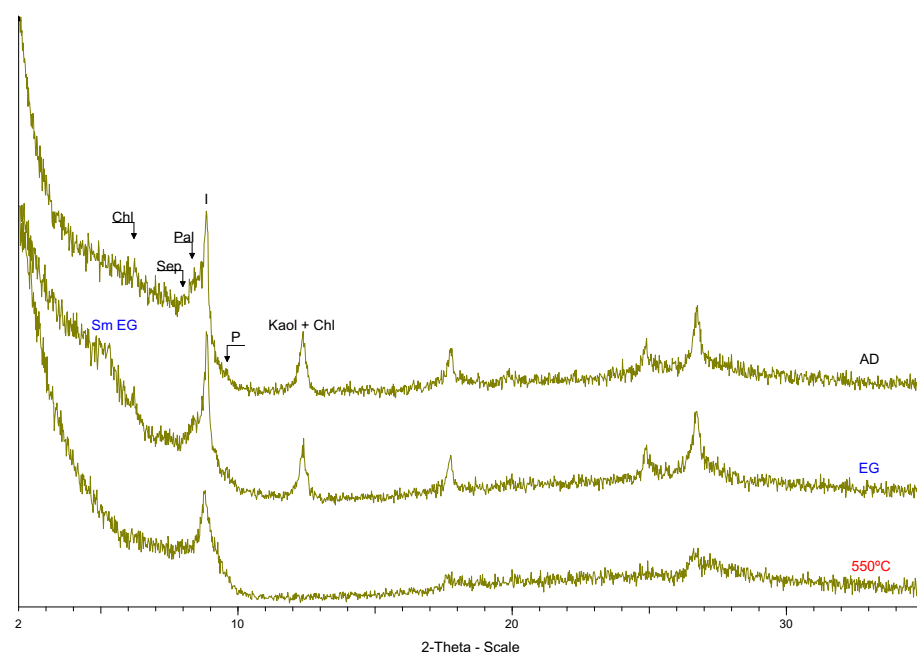


Fig. 7. XRD patterns of oriented mounts of a representative sample (AC): air dried (AD), ethylene glycol solvated (EG) and thermal treated (550 °C). The clay mineral assemblage comprise: sepiolite (Sep), palygorskite (Pal), illite (I), pyrophyllite (Prl), kaolinite (Kaol), chlorite (Chl) and smectites (Sm). Notice the broaden peaks of Pal, Sep and Sm (only perceived on EG pattern).

Table 4

Clay mineralogy: semi quantification results obtained by XRD oriented mounts method. With exception of Prl, Pyrophyllite; according to [Whitney and Evans \(2010\)](#). The rest of clay minerals have the following abbreviations: I, Illite; Chl, Chlorite; Kaol, Kaolinite; Pal, Palygorskite; Sep, Sepiolite; and Sm, Smectite. (-) Not detected. TOC: total organic carbon.

Sample	Location/type	Fraction	I	Chl	Kaol	Prl	Pal	Sep	Sm	TOC
			%w/w	%w/w	%w/w	%w/w	%w/w	%w/w	%w/w	%
LG-2	Mudflat trench	< 0,5 µm	38	4	5	1	33	11	8	-
		< 2 µm	62	22	3	1	3	6	4	-
LG-3	Mudflat trench	< 0,5 µm	28	11	10	-	29	15	6	-
		< 2 µm	48	6	4	-	27	9	7	-
LG-4	Mudflat trench	< 0,5 µm	94	-	6	-	-	-	-	-
		< 2 µm	79	3	3	-	8	6	1	-
LG-5	Mudflat trench	< 0,5 µm	13	14	5	-	49	15	4	-
		< 2 µm	46	8	7	4	15	15	6	-
LG-5b	Mudflat trench	< 0,5 µm	62	8	3	2	13	8	5	-
		< 2 µm	71	2	2	1	17	5	2	-
LG-6	Mudflat trench	< 0,5 µm	16	22	8	5	12	21	16	-
		< 2 µm	33	8	7	2	22	22	6	-
MC-LG	Surficial mat curls	< 0,5 µm	37	5	23	2	10	8	16	-
		< 2 µm	36	1	10	5	9	14	26	-
MF-LG	Surficial decaying mat	< 0,5 µm	9	2	9	5	14	13	48	-
		< 2 µm	30	4	11	5	18	7	26	-
AG S1 0-2	Shore core	< 2 µm	27	1	15	-	2	-	55	-
AG S1 12-15	Shore core	< 2 µm	21	6	8	-	16	49	-	0.5 ± 0.1
AG S2 6-8	Shore core	< 2 µm	47	5	15	-	8	26	-	-
AG S3 0-2	Shore core	< 2 µm	37	0	25	-	3	34	-	-
AG S3 2-4	Shore core	< 2 µm	16	4	11	-	5	64	-	0.8 ± 0.1
AG S3 4-6	Shore core	< 2 µm	16	1	5	-	2	73	3	-
AG S3 6-8	Shore core	< 2 µm	4	1	5	-	-	86	3	0.5 ± 0.1
AG S3 10-13	Shore core	< 2 µm	7	1	3	-	2	85	2	-
AG SB 6-8	Inner core	< 2 µm	37	8	27	-	17	7	12	0.5 ± 0.1
AG SB 14-16	Inner core	< 2 µm	31	2	26	-	7	13	23	0.4 ± 0.1
AG SB 20-22	Inner core	< 2 µm	61	6	15	-	5	2	17	-
AG SB 26-28	Inner core	< 2 µm	90	3	10	-	-	-	-	0.7 ± 0.1
AG SB 32-34	Inner core	< 2 µm	21	2	6	-	24	50	-	-
MC-AG	Surficial mat curls	< 0,5 µm	5	7	22	-	33	34	-	-
		< 2 µm	10	1	13	3	11	11	50	-
ALTC	Surficial porous sediment	< 0,5 µm	6	9	19	-	34	31	-	-
		< 2 µm	24	1	8	2	3	6	55	-

microbial mats develop. Upon burial and facilitated by sufficient Mg^{2+} in solution, clay crystallization proceeds even though the composition and structure of the resulting phase depend on the pore fluid chemistry, which is greatly variable.

The overall abundance of the clay minerals also varies through the

different sedimentary facies reflecting changes in the environmental conditions (evaporation, detrital input, bioturbation, desiccation, reworking, etc.). In general, the highest concentrations of Mg-clays have been determined in burrowed beds, desiccated mat curls and sediment showing vesicular structure. These structures have in common that their formation

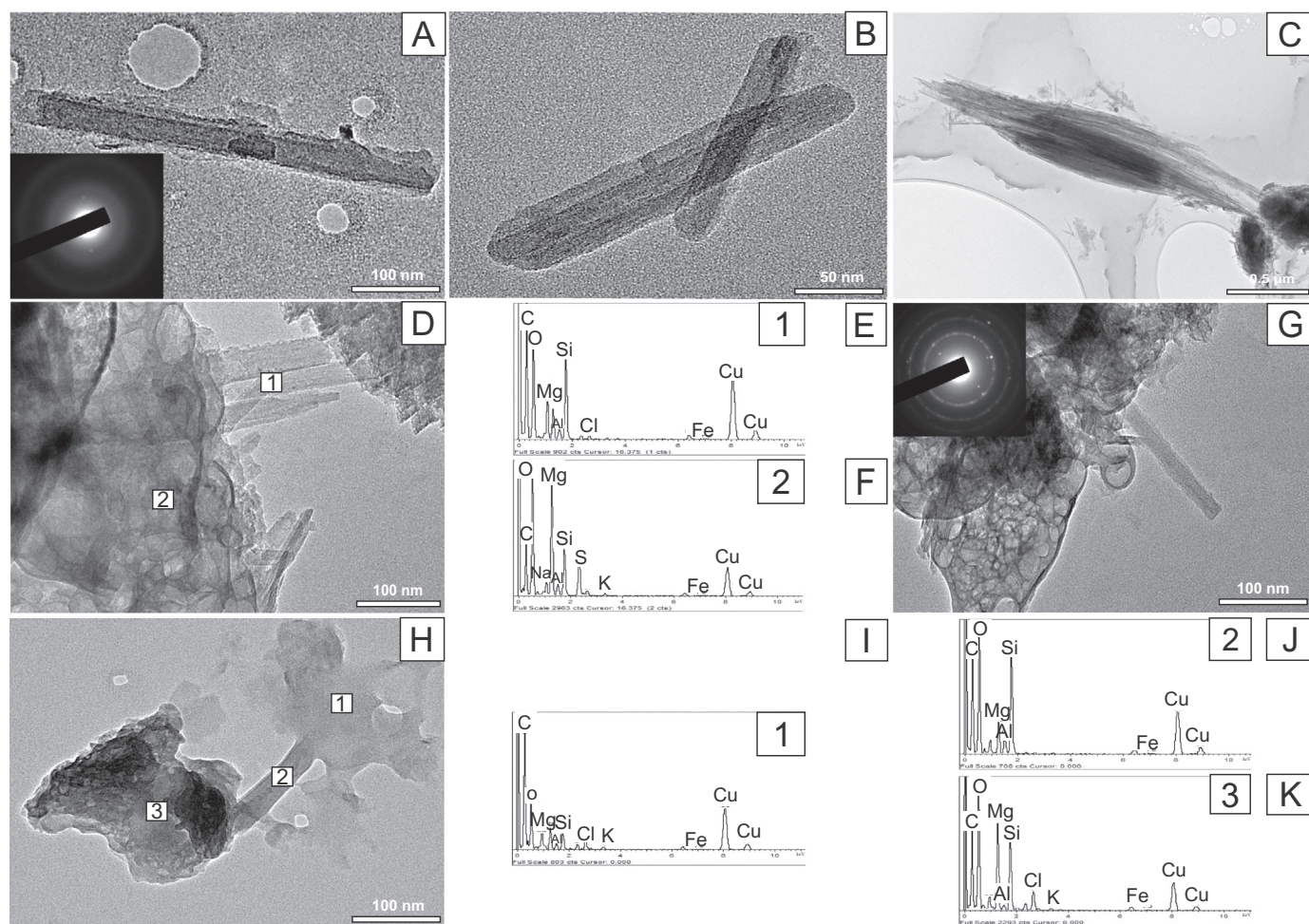


Fig. 8. TEM micrographs, SAED patterns and AEM analysis of Pal-Sep crystals and associated EPS. A: Nanometer-sized Pal lath that produces a poorly crystalline diffraction pattern (SAED). B: Rods of common Pal. C: Fibers of pure Sep aggregated into a bundle. D: Hydrated and turgent EPS with an alveolar structure that contain an array of fibers protruding outwards. Mg is adsorbed to the EPS in much higher amounts than the associated ions, see EDXS of point 2 (F). The composition of the fibers in point 1 (E) is consistent with a Pal mineralogy. G: The occurrence of several crystals of Pal randomly embedded by the EPS produces a polycrystalline diffraction pattern (SAED). H: A gradation of EPS structures from alveolar (3) to flat and massive (1) is produced as the EPS dehydrate. The shrunk parts are connected by fibers of Pal composition (J). Notice that the concentration of ions adsorbed to the dehydrated EPS (I) is much lower than in the hydrated and Mg-rich parts (K).

enhances the degradation of microbial mats. Alternatively, the permanent or seasonal character of the lake in combination with the central or marginal location of the deposit has effect on the type and amount of the associated evaporites that may play a control on clay authigenesis. In fact, the precipitation of a hydrous magnesium sulfate such as epsomite in LG seems to prevent the formation of the fibrous silicates since requires high concentration of Mg. By contrast, the occurrence of gypsum and other evaporites does not appear to influence the relative abundance of the authigenic clay minerals.

5.2. Clay crystallization on EPS

In the study playa lakes, microbial mats consist of cyanobacterial and diatoms that develop on the surface of the submerged sediment, infilling the interparticle spaces by the extracellular polymeric substances (EPS) secreted by themselves. As the microorganisms grow they alter the detrital grains by degrading them physical and chemically. The microbial degradation of the silicate minerals (I, Chl, Prl, Kaol, Qz and Fsp) is generalized but, as explained above, affects preferentially the phyllosilicates that are commonly found disaggregated (Fig. 6D). Microbes attach selectively to the phyllosilicates because they have a large surface area (Alimova et al., 2009) and contain beneficial nutrients such as Fe and K (Rogers and Bennett, 2004; Sanz-Montero et al., 2009b; Sanz-Montero and Rodríguez-Aranda, 2009). The dissolution of the

detrital silicates enables the release of ions (Si, Al, K, Fe, etc.) that are shown to be fixed to the EPS (Fig. 8K). Mg and, to a minor extent, Ca are found in high concentrations in the water solutions (Table 1) and get fixed to the EPS due to its affinity for divalent cations (Dupraz and Visscher, 2005). The result is a heterogeneous matrix where variable amounts of amorphous to crystalline (Mg-Al)-Si phases coexist, along with other authigenic minerals, mainly, gypsum, calcite and aragonite. The creation of poorly ordered, Mg-Si phases is common in modern microbial mats (Konhauser and Ferris, 1996; Souza-Egipsy et al., 2005; Zeyen et al., 2015; Pace et al., 2016) and can be preserved in ancient lacustrine microbialites (Sanz-Montero et al., 2008).

Pal laths exhibiting incipient faces (Fig. 6E) are the first nanometer-sized crystals forming on the EPS. The mixture of randomly-oriented and nanometer-sized crystals with amorphous phases explains the polycrystalline condition of the EPS (Fig. 8F). Chemical and textural evolution of EPS caused by dehydration confirms a continuum between ionic chelation and clay nucleation in the organic templates. The Mg-clays represent intermediate phases in the gradual transition from turgent EPS, containing Mg and other ions strongly attached, to collapsed and massive EPS with low amount of charge. The dehydration of the EPS entails the release of Mg and its enrichment in the remaining adsorbed ions, mostly Si. Along this line, L  veill   et al. (2000) claimed that desiccation of EPS was involved in the formation of kerolite in microbial mats and Konhauser and Urrutia (1999) had

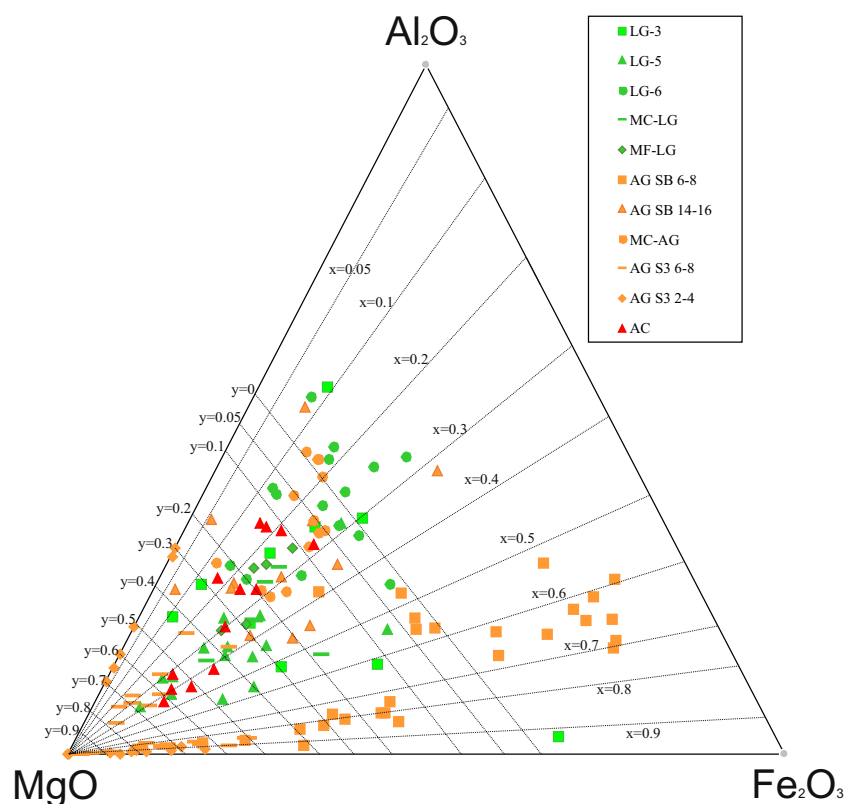


Fig. 9. AEM analysis of Pal and Sep plotted in the ternary graph modified from Suárez and García-Romero (2013). See the location of the samples in Figs. 2–5.

suggested that upon EPS desiccation, precursors dehydrated and transformed into more stable ordered clays. In the same way, Ueshima and Tazaki (2001) suggested that the formation of Sm took place in EPS that acted as charged templates.

In the study playa lakes, the largest accumulations of the magnesian phyllosilicates found in the dry mat curls and bioturbated microbial mats support that the degradation of the microbial biomass by dehydration play a key role on clay authigenesis in this type of shallow sedimentary system. Extracellular polymeric substances (EPS) produced in microbial mats which may act both as templates and reservoir of Si, Al, and other ions, which favors the silicate formation.

5.3. Implications for the rock record

The interplay between microorganisms and Mg-clay formation is increasingly being investigated both in natural and in experimental systems but mostly focused on Sm and kerolite (Ueshima and Tazaki, 2001; Zeyen et al., 2015). To the best of our knowledge this is the first work that reports the biomediated nucleation of Pal-Sep on EPS and provides an excellent analogue for better understanding the ancient sedimentary environments of the fossil counterparts that can be traced back at least to the Neoproterozoic (Mettraux et al., 2015). Our results confirm previous environmental interpretations done from sedimentary sequences (Calvo et al., 1999; Galán and Pozo, 2011; Calvo and Pozo, 2013) but also clarify important issues concerning Si availability in pore water as well as the crucial role of microorganisms both in the destruction and production of silicates.

6. Conclusions

Authigenic Mg-clays assemblages comprised of Pal-Sep and Sm are forming in microbial mats hosted in Si-poor and Mg-rich playa lakes from Central Spain.

The formation of the Mg-clays occurs on extracellular polymeric

substances (EPS) of microbial mats that act both as templates and reservoir of Si, Al, and other ions. Thus, even in ephemeral saline systems binding and ion exchange mechanisms in microbial mats are involved into the rapid cycling of silicon through the destruction and neoformation of silicates.

The bioinduced crystallization tends to follow a pattern from the very small and poorly ordered phases to more ordered crystals favored by the progressive desiccation of the EPS. In first stages, small sized and poorly ordered laths of pure Pal nucleate in relation with the EPS. Additional growing of the crystals results in larger fibers of Mg- Pal to Al- Sep phases. At a final growing stage, the aggregation of several fibers resulted in the formation of bundles of pure Sep.

The extensive occurrence of bioinduced Mg-clays in the microbial sediment shows that this type of silicate mineralization is a common process that can enhance the preservation of the microbial structures in ancient evaporitic rocks.

Acknowledgements

This research work has been funded by the Spanish Ministry of Economy and Competitiveness through National Research Project CGL2015-66455-R (MINECO-FEDER). We wish to thank all the members of the Project for their help and learnings. We also thank Dr. R. Martos for assistance with the mineralogical work. It is part of the scientific activities of Research Group UCM-910404. P. Del Buey acknowledges support from a Predoctoral Grant (CT27/16-CT28/16 UCM). The authors thank the Associate Editor of Applied Clay Science, E. Galán, for his editorial work. We are grateful to two anonymous reviewers who contributed to the improvement of the manuscript.

Appendix A. Supplementary data

Supplementary data to this article can be found online at <https://doi.org/10.1016/j.clay.2018.02.020>.

References

- Alimova, A., Katz, A., Steiner, N., Rudolph, E., Wei, H., Steiner, J.C., Gottlieb, P., 2009. Bacteria-clay interaction: structural changes in smectite induced during biofilm formation. *Clay Clay Miner.* 57, 205.
- Birsoy, R., 2002. Formation of sepiolite-palygorskite and related minerals from solution. *Clay Clay Miner.* 50, 736–745.
- Bustillo Revuelta, M.A., García-Romero, E., 2003. Arcillas fibrosas anómalas en entornos de sedimentos superficiales: características y génesis (Esquivias, Cuenca de Madrid). *Boletín de la Sociedad Española de Cerámica y Vidrio* 42, 289–297.
- Cabestrero, Ó., Sanz-Montero, M.E., 2018. Brine evolution in two inland evaporative environments: influence of microbial mats in mineral precipitation. *J. Paleolimnol.* 59 (2), 139–157.
- Cabestrero, Ó., García Del Cura, M.A., Sanz-Montero, M.E., 2013. Precipitación de sales en una laguna sulfatada magnésico-sódica (Lillo, Toledo): controles ambientales. *Macla* 17, 27–28.
- Cabestrero, Ó., Arroyo, X., García Del Cura, M.A., Sanz-Montero, M.E., 2014a. Formación de arcillas en lagunas sulfatadas efímeras (Lillo, Toledo). *Macla* 19.
- Cabestrero, Ó., Sanz-Montero, M.E., García Del Cura, M.A., 2014b. Precipitation of magnesium bearing-sulphates in saline lakes: influence of sedimentary structures and microbial processes. In: 19th International Sedimentological Congress, Geneva, Switzerland, pp. 18–22.
- Cabestrero, Ó., Del Buey, P., Sanz-Montero, M.E., 2016. Geochemical modelling of the precipitation processes in SO_4 -Mg/Na microbialites. *Macla* 21, 20–21.
- Cabestrero, Ó., Del Buey, P., Sanz-Montero, M.E., 2018. Biosedimentary and geochemical constraints on the precipitation of mineral crusts in shallow sulphate lakes. *Sediment. Geol.* 366, 32–46. <http://dx.doi.org/10.1016/j.sedgeo.2018.01.005>.
- Calvo, J.P., Pozo, M., 2013. Geology of magnesium clays in sedimentary and non-sedimentary environments. In: Pozo, M., Galán, E. (Eds.), *Magnesian Clays: Characterization, Origin & Applications*. AIPEA Educational Series, vol. 2 (Bari (Italy) (Chapter 3)).
- Calvo, J.P., Blanc-Valleron, M.M., Rodríguez-Aranda, J.P., Rouchy, J.M., Sanz-Montero, M.E., 1999. Authigenic Clay Minerals in Continental Evaporitic Environments, Palaeoweathering, Palaeosurfaces and Related Continental Deposits. Blackwell Publishing Ltd., pp. 129–151.
- Chung, F.H., 1974. Quantitative interpretation of X-ray diffraction patterns. I. Matrix flushing method for quantitative multicompetent analysis. *J. Appl. Crystallogr.* 7, 519–525.
- Cölfen, H., Antonietti, M., 2008. *Mesocrystals and Nonclassical Crystallization*. Wiley, Chichester, England (276 pp).
- Cuevas, J., Leguey, S., Ruiz, A.I., 2011. Evidence for the biogenic origin of Sepiolite. In: Galán, E., Singer, A. (Eds.), *Developments in Palygorskite-Sepiolite Research. A New Outlook on these Nanomaterials*. Developments in Clay Science 3. Elsevier, pp. 219–235 Amsterdam. (Chapter 9).
- Del Buey, P., Cabestrero, O., Sanz-Montero, M.E., 2016. New insights into the bioinduced precipitation of hydrated sulfates in hypersaline microbialites. *Macla* 21, 25–26.
- Dupraz, C., Visscher, P.T., 2005. Microbial lithification in marine stromatolites and hypersaline mats. *Trends Microbiol.* 13, 429–438.
- Ferris, F.G., Fyfe, W.S., Beveridge, T.J., 1987. Bacterial as nucleation sites for authigenic minerals in a metal-contaminated lake sediment. *Chem. Geol.* 63, 225–232.
- Galán, E., Pozo, M., 2011. Palygorskite and Sepiolite deposits in continental environments. Description, genetic patterns and sedimentary settings. In: Galán, E., Singer, A. (Eds.), *Developments in Palygorskite-Sepiolite Research. A New Outlook on these Nanomaterials*. Developments in Clay Science, vol. 3. Elsevier, pp. 125–166 Amsterdam. (Chapter 6).
- García-Romero, E., Suárez, M., 2013. Sepiolite-palygorskite: textural study and genetic considerations. *Appl. Clay Sci.* 86, 129–144.
- García-Romero, E., Suárez, M., 2014. Sepiolite-palygorskite polysomatic series: oriented aggregation as a crystal growth mechanism in natural environments. *Am. Mineral.* 99, 1653.
- García-Romero, E., Suárez, M., Bustillo-Revuelta, M.A., 2004. Characteristics of a Mg-Palygorskite in Miocene rocks, Madrid basin (Spain). *Clay Clay Miner.* 52, 484–494.
- Jackson, M.L., 1979. *Soil Chemical Analysis –Advanced Course*. (Madison, Wisconsin, 895 pp).
- Jones, B.F., 1983. Occurrence of clay minerals in surficial deposits of southwestern Nevada. *Sci. Geol. Miner.* 72, 81–92.
- Jones, B.F., Deocampo, D.M., 2003. Saline lakes. In: Drever, J.I. (Ed.), *Surface and Ground Water, Weathering, Erosion and Soils. Treatise on Geochemistry* pp. 393–424.
- Jones, B.F., Galán, E., 1988. Sepiolite and palygorskite. *Rev. Mineral. Geochem.* 19, 631.
- Khademi, H., Mermut, A.R., 1998. Source of palygorskite in gypsiferous Aridisols and associated sediments from central Iran. *Clay Miner.* 33, 561–578.
- Konhauser, K.O., Ferris, F.G., 1996. Diversity of iron and silica precipitation by microbial mats in hydrothermal waters, Iceland: implications for Precambrian iron formations. *Geology* 24, 323–326.
- Konhauser, K.O., Urrutia, M.M., 1999. Bacterial clay authigenesis: a common biogeochemical process. *Chem. Geol.* 161, 399–413.
- Konhauser, K.O., Fyfe, W.S., Ferris, F.G., Beveridge, T.J., 1993. Metal sorption and mineral precipitation by bacteria in two Amazonian river systems: Rio Solimões and Rio Negro, Brazil. *Geology* 21 (12), 1103–1106.
- Kübler, K., 1987. Cristallinité de l'illite, méthodes normalisées de préparations, méthodes normalisées de mesure. *Série ADX Cahiers Institut de Géologie de Neuchâtel* (13 p).
- Leguey, S., Ruiz De León, D., Ruiz, A.I., Cuevas, J., 2010. The role of biomineralization in the origin of sepiolite and dolomite. *Am. J. Sci.* 310, 165–193.
- Léveillé, R.J., Fyfe, W.S., Longstaffe, F.J., 2000. Geomicrobiology of carbonate-silicate microbialites from Hawaiian basaltic sea caves. *Chem. Geol.* 169, 339–355.
- Mettraux, M., Homewood, P., Dos Anjos, C., Erthal, M., Lima, R., Matsuda, N., Souza, A., Al Balushi, S., 2015. Microbial communities and their primary to early diagenetic mineral phases; the record from Neoproterozoic microbialites of Qarn Alam, Oman. *Geol. Soc. Lond., Spec. Publ.* 418, 123.
- Meunier, A., 2005. *Clays*. Springer (472 pp).
- Moore, D.M., Reynolds, R.C., 1997. *X-Ray Diffraction and the Identification and Analysis of Clay Minerals*. (Oxford. 378pp).
- Navarro, J.B., Moser, D.P., Flores, A., Ross, C., Rosen, M.R., Dong, H., Zhang, G., Hedlund, B.P., 2008. Bacterial succession within an ephemeral hypereutrophic Mojave Desert playa Lake. *Microb. Ecol.* 57, 307–320.
- Nieto, F., Arroyo, F., Aróstegui, J., 2016. XRD-TEM-AEM comparative study of n-alkylammonium smectites and interstratified minerals in shallow-diagenetic carbonate sediments of the Basque-Cantabrian Basin. *Am. Mineral.* 101, 385–398.
- Pace, A., Bourillot, R., Bouton, A., Vennin, E., Galaup, S., Bundeleva, I., Patrier, P., Dupraz, C., Thomazo, C., Sansjofre, P., Yokoyama, Y., Franceschi, M., Anguy, Y., Pigot, L., Virgone, A., Visscher, P.T., 2016. Microbial and diagenetic steps leading to the mineralisation of Great Salt Lake microbialites. *Sci. Rep.* 6, 31495.
- Pozo, M., Casas, J., 1999. Origin of kerolite and associated Mg clays in palustrine-lacustrine environments. The Esquivias deposit (Neogene Madrid Basin, Spain). *Clay Miner.* 34, 395–418.
- Rodríguez-Aranda, J.P., Sanz-Montero, M.E., Cabestrero, O., 2014. Burrowing beetles in saline lake shores: effects on the preservation of mat-related structures. In: 19th International Sedimentological Congress, Geneva, Switzerland.
- Rogers, J.R., Bennett, P.C., 2004. Mineral stimulation of surface microorganisms: release of limiting nutrients from silicates. *Chem. Geol.* 203, 91–108.
- Sánchez, C., Galán, E., 1995. An approach to the génesis of palygorskite in a Neogene-quaternary continental basin using principal factor analysis. *Clay Miner.* 30, 225–238.
- Sanz-Montero, M.E., Rodríguez-Aranda, J.P., 2009. Silicate bioweathering and biomineralization in lacustrine microbialites: ancient analogues from the Miocene Duero Basin, Spain. *Geol. Mag.* 146, 527–539.
- Sanz-Montero, M.E., Rodríguez-Aranda, J.P., 2013. The role of microbial mats in the movement of stones on playa lake surfaces. *Sediment. Geol.* 298, 53–64.
- Sanz-Montero, M.E., Rodríguez-Aranda, J.P., García Del Cura, M.A., 2009a. Dolomite-silica stromatolites in Miocene lacustrine deposits from the Duero Basin, Spain: the role of organotemplates in the precipitation of dolomite. *Sedimentology* 55, 729–750.
- Sanz-Montero, M.E., Rodríguez-Aranda, J.P., García Del Cura, M.A., 2009b. Bioinduced precipitation of barite and celestite in dolomite microbialites examples from Miocene lacustrine sequences in the Madrid and Duero Basins, Spain. *Sediment. Geol.* 222, 138–148.
- Sanz-Montero, M.E., Rodríguez-Aranda, J.P., Perez-Soba, C., 2009b. Microbial weathering of Fe-rich phyllosilicates and formation of pyrite in the dolomite precipitating environment of a Miocene lacustrine system. *Eur. J. Mineral.* 21, 163–175.
- Sanz-Montero, M.E., Calvo, J.P., García del Cura, M.A., Ornos, C., Outerelo, R., Rodríguez-Aranda, J.P., 2013a. The rise of the dipterid-microbial mat interactions during the Cenozoic: consequences for the sedimentary record of saline lakes. *Terra Nova* 25, 465–471.
- Sanz-Montero, M.E., Arroyo, X., Cabestrero, Ó., Calvo, J.P., Fernández-Escalante, E., Fidalgo, C., García del Cura, M.A., García-Avilés, J., González-Martín, J.A., Rodríguez-Aranda, J.P., Rovira, J.V., 2013b. Procesos de sedimentación y biomineralización en la laguna alcalina de las Eras (Humedal Coca-Olmedo). *Geogaceta* 53, 97–100.
- Sanz-Montero, M.E., Cabestrero, O., Rodríguez-Aranda, J.P., 2015a. Gypsum microbialites and mat-related structures in shallow evaporitic lakes. *Geol. Surv.* 189–190.
- Sanz-Montero, M.E., Cabestrero, O., Rodríguez-Aranda, J.P., 2015b. Sedimentary effects of flood-producing windstorms in playa lakes and their role in the movement of large rocks. *Earth Surf. Process. Landf.* 40, 864–875.
- Singer, A., 1989. Palygorskite and sepiolite group minerals. In: Weed, J.B.D.S.B. (Ed.), *Minerals in Soil Environments*, Soil Sci. Soc. Am. Madison, WI. pp. 829–872.
- Souza-Egipsy, V., Wierchos, J., Ascaso, C., Neelson, K.H., 2005. Mg-silica precipitation in fossilization mechanisms of sand tufa endolithic microbial community, mono Lake (California). *Chem. Geol.* 217, 77–87.
- Suárez, M., García-Romero, E., 2011. Advances in the crystal chemistry of sepiolite and palygorskite. In: Galán, E., Singer, A. (Eds.), *Developments in Palygorskite-Sepiolite Research. A New Outlook on these Nanomaterials*. Developments in Clay Science, vol. 3. Elsevier, pp. 33–55 Amsterdam. (Chapter 2).
- Suárez, M., García-Romero, E., 2013. Sepiolite-Palygorskite: a continuous polysomatic series. *Clay Clay Miner.* 61, 461.
- Suárez, M., Robert, M., Elsaass, F., Martín Pozas, J.M., 1994. Evidence of a precursor in the neof ormation of palygorskite - new data by analytical electron microscopy. *Clay Miner.* 29, 255–264.
- Tazaki, K., 1997. Biomineralization of layer silicates and hydrated Fe/Mn oxides in microbial mats: an electron microscopical study. *Clay Clay Miner.* 45, 203–212.
- Tosca, N.J., Masterson, A.L., 2014. Chemical controls on incipient Mg-silicate crystallization at 25°C: implications for early and late diagenesis. *Clay Miner.* 49, 165.
- Ueshima, M., Tazaki, K., 2001. Possible role of microbial polysaccharides in nontronite formation. *Clay Clay Miner.* 49, 292.
- Whitney, D.L., Evans, B.W., 2010. Abbreviations for name of rock-forming minerals. *Am. Mineral.* 95, 185–187.
- Zeyen, N., Benzerara, K., Li, J., Groleau, A., Balan, E., Robert, J.L., Estève, I., Tavera, R., Moreira, D., López-García, P., 2015. Formation of low-T hydrated silicates in modern microbialites from Mexico and implications for microbial fossilization. *Front. Earth Sci.* 3.